Cellular uptake of rose bengal is mediated by OATP1B1/1B3 transporters

Journal Pre-proofs

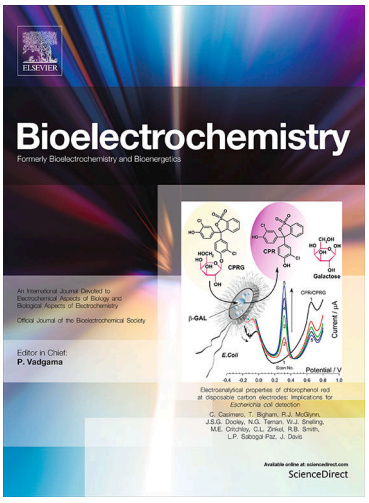

Cellular uptake of rose bengal is mediated by OATP1B1/1B3 transporters

K. Sztandera, M. Gorzkiewicz, E.A. Zizzi, N. Dybczak, L. Poltorak, M.A. Deriu, B. Klajnert-Maculewicz

PII: S1567-5394(23)00086-5
DOI: https://doi.org/10.1016/j.bioelechem.2023.108449
Reference: BIOJEC 108449

To appear in: *Bioelectrochemistry*

Received Date: 10 January 2023
Revised Date: 22 March 2023
Accepted Date: 17 April 2023

Please cite this article as: K. Sztandera, M. Gorzkiewicz, E.A. Zizzi, N. Dybczak, L. Poltorak, M.A. Deriu, B. Klajnert-Maculewicz, Cellular uptake of rose bengal is mediated by OATP1B1/1B3 transporters, *Bioelectrochemistry* (2023), doi: https://doi.org/10.1016/j.bioelechem.2023.108449

Cellular uptake of rose bengal is mediated by OATP1B1/1B3 transporters

K. Sztandera[1§], M. Gorzkiewicz[1,2*§], E. A. Zizzi[3], N. Dybczak[4], L. Poltorak[4], M. A. Deriu[3], B. Klajnert-Maculewicz[1]

[1] *Department of General Biophysics, Faculty of Biology and Environmental Protection, University of Lodz, 141/143 Pomorska St., 90-236 Lodz, Poland.*

[2] *Department of Molecular Medicine II, Medical Faculty, Heinrich Heine University Düsseldorf, Universitätsstr. 1, 40225 Düsseldorf, Germany*

[3] *PolitoBIOMedLab, Department of Mechanical and Aerospace Engineering, Politecnico di Torino, Corso Duca degli Abruzzi 24, 10129 Turin, Italy*

[4] *Department of Inorganic and Analytical Chemistry, Faculty of Chemistry, University of Lodz, Tamka 12, 91-403, Lodz, Poland*

*corresponding author: michal.gorzkiewicz@biol.uni.lodz.pl

§ These authors contributed equally to this work.

Abstract:

Due to its fluorescent properties and high yield of singlet oxygen, rose bengal (RB) is one of the most promising photosensitizers for cancer treatment. However, the negative charge of RB molecule may significantly hamper its intracellular delivery by passive diffusion through the cell membrane. Thus, specific membrane protein transporters may be needed. The organic anion transporting polypeptides (OATPs) family are a well-characterized group of membrane protein transporters, responsible for cellular uptake of a number of drugs. To our knowledge, this is the first study that evaluates cellular transport of RB mediated by the OATP transporter family.

First, electrified liquid-liquid interface, together with biophysical analysis and molecular dynamics simulations were used to characterize the interaction of RB with several models of a cellular membranes. These experiments proved that RB interacts only with the membrane's surface, without spontaneously crossing the lipid bilayer. Evaluation of intracellular uptake of RB by flow cytometry and confocal microscopy showed significant differences in uptake between liver and intestinal cell line models differing in expression of OATP transporters. The use of specific pharmacological inhibitors of OATPs, together with Western blotting and in silico analysis, indicated that OATPs are crucial for cellular uptake of RB.

Keywords: Rose bengal, intracellular uptake, organic anions transporters, liquid-liquid interface, electrochemistry

1. Introduction

Rose bengal (4,5,6,7-tetrachloro-2',4',5',7'-tetraiodofluorescein, RB) is a water-soluble, dianionic fluorescein derivative that functions as an organic fluorescent dye and belongs to the xanthene family of synthetic dyes [1]. Originally used as a wool colorant, RB has been subsequently approved as a food dye, and is also used in ophthalmology to stain damaged conjunctiva and cornea [2]. Due to its fluorescent properties and high yield of singlet oxygen, RB has been proposed as a photosensitizer in photodynamic therapy [3–6]. However, its shortcomings include its hydrophilic nature, negative charge, tendency to aggregate, and short half-life time, which hinder the transmembrane cellular uptake of RB, and consequently, the efficiency of RB treatments [7]. In addition, the mechanism of cellular uptake of RB remains poorly understood; therefore, current studies focus on the application of nanocarriers to overcome these obstacles [1].

The three main pathways of transmembrane transport of low molecular weight compounds are as follows: diffusion, assisted transport, and active transport. The type of transport depends on the properties of the compound such as its shape, charge, and size. The cell membrane components contain negatively charged phosphate groups; therefore, hydrophilic and negatively charged molecules require membrane protein transporters for cellular entry [8]. The organic anion transporting polypeptide (OATP) family is a well-characterized group of membrane protein transporters, coded by solute carrier family (SLC) genes. OATPs are multi-specific transporters that mediate the transport of various compounds including xenobiotics (OATP1A2) and prostaglandins (OATP2A1). This transport is ATP- and sodium-independent; however, the exact mechanism remains under evaluation [9]. To date, more than 300 OATPs have been reported, 11 of which are expressed in human tissues. OATPs are divided into six families according to their amino acid sequence; they consist of 643 to 724 amino acids and possess 12 transmembrane domains [9]. Depending on the type, OATPs occur primarily in the brain, heart, testis, kidney, and liver, where they are located mainly in epithelial cells.

To the best of our knowledge, this is the first study that evaluates cellular transport of RB mediated by the OATP transporter family. An electrified liquid-liquid interface was used to assess the interaction of RB with the soft junction as a basic model of a cell surface. Electroanalytical tools were used to evaluate the physicochemical parameters (e.g., water-1,2-dichloroethane partition coefficient, diffusion coefficient) related to RB together with the mechanism of interfacial transport. Biophysical analysis showed that RB at low concentrations could not interact with negatively charged micelles, at the same time interacting to a limited extent with the cell membrane surface; the latter was confirmed by molecular dynamics (MD) simulations. Therefore, it was concluded that RB cannot cross the cellular membrane, suggesting the requirement for membrane transporters. Evaluation of intracellular uptake of RB by flow cytometry and confocal microscopy showed significant differences in uptake between cancer cell lines expressing different levels of OATP transporters. The application of specific pharmacological inhibitors of OATPs, together with Western blotting and in silico analysis, indicated that OATPs are crucial for cellular uptake of RB.

2. Materials and Methods

2.1. Materials

RB, fetal bovine serum, penicillin/streptomycin solution, trypsin-EDTA solution, MTT (3-(4,5-dimethyl-2-thiazolyl)-2,5-diphenyl-2H-tetrazolium bromide), lipopolysaccharides from Escherichia coli O111:B4 (LPS), cyclosporin A, rifampicin, budesonide, pravastatin, naringin, taurocholic acid, allura red, and ritonavir were purchased from Sigma-Aldrich (Taufkirchen, Germany). Dulbecco's phosphate buffered saline with no calcium and magnesium (DPBS) was purchased from Biowest (France). DMEM and RPMI culture media was obtained from Gibco, Thermo Fisher Scientific (Waltham, Massachusetts, USA). Dimethyl sulfoxide (DMSO) was purchased from POCH (Gliwice, Poland). Cell lines (HepG2, Hep3B, HT-29, and Caco-2) were obtained from ATCC. For the experiments involving the electrified liquid-liquid interface, the aqueous phase was a solution of 10 mM NaCl (analytical grade, POCH) or Britton-Robinson buffer (mixture of 10 mM phosphoric acid,

10 mM boric acid, and 10 mM acetic acid), which was pH adjusted with 1 M HCl or 1 M NaOH. The organic phase solvent was 1,2-dichloroethane (1,2-DCE, 99%, Sigma). Bis(triphenylphosphoranylidene)ammonium tetrakis(4-chlorophenyl)borate was used as the organic phase background electrolyte salt, was synthesized from bis(triphenylphosphoranylidene)ammonium chloride (BTPPACl; 97%, Sigma-Aldrich) and potassium tetrakis(4-chlorophenyl)borate (>98%, Sigma-Aldrich); its concentration was maintained at 5 mM in all measurements.

2.2. Electrified liquid-liquid interface

The behavior of RB at the electrified liquid-liquid interface was studied in a traditional four-electrode cell (glass tube equipped with two Luggin capillaries) with the Autolab 302n potentiostat. Two reference (Ag/AgCl wires) and two counter (Pt wires) electrodes were used to measure the interfacial potential drop and impose interfacial potential difference, respectively. The organic phase reference electrode was additionally immersed in the 10 mM BTPPACl and 10 mM NaCl aqueous solution placed into the longer Luggin capillary. The organic phase counter electrode was insulated with the glass within the section remaining in direct contact with the aqueous phase. Potentiostatic cyclic voltammetry was employed as the electroanalytical tool. The experiential scan rate was 20 mV/s unless indicated otherwise. The recorded ionic current corresponded to the interfacial charge transfer reactions: transfer of the anion from the aqueous to the organic phase (negative current); transfer of the anion from the organic to the aqueous phase (positive current); transfer of the cation from the organic to the aqueous phase (negative current); and transfer of the cation from the aqueous to the organic phase (positive current). During all experiments the direction of polarization was from less positive to more positive potential difference values on the forward scan. Each recorded curve was recorded at least five times without any preconditioning time applied between consecutive cycles. First and the last curve were always discarded. Whenever the $\Delta\phi$ is used as the x axis descriptor the potential difference was calibrated to the standard transfer of the TMA^+ (model ion). For the cyclic voltammograms having "potential" in the axis label the voltammograms are given on the applied potential difference scale.

2.3. Hydrodynamic diameter measurements

Measurements of hydrodynamic diameter were performed by the Dynamic Light Scattering method (DLS) on a Zetasizer Nano ZS instrument (Malvern Instruments Ltd, Malvern, UK). LPS (from *E. coli*) was dissolved in PBS (10 mM, pH 7.4) to a final concentration of 100 μg/mL. The solutions were placed in low volume sizing cuvettes (ZEN0112, Malvern Instruments Ltd., Malvern, UK) and the size of the formed micelles was measured. RB solution was then added to obtain given concentrations and the hydrodynamic diameter was measured immediately. The data were analyzed using Malvern software.

2.4. Cell culture

The Caco-2, HepG2, and Hep3B cell lines were cultured in DMEM medium, and the HT-29 cell line was cultured in RPMI medium. Both media contained 1% penicillin/streptomycin and 10% heat-inactivated FBS. Cells were cultured in T-75 culture flasks at 37 °C/5% CO_2 and sub-cultured every 3 days. Cells were harvested using 0.25% (w/v) trypsin-0.03% (w/v) EDTA. The number of viable cells was determined with the Trypan blue exclusion assay on a Countess Automated Cell Counter (Invitrogen, Carlsbad, CA, USA).

2.5. Fluorescence anisotropy

HT-29, Caco-2, HepG2, and Hep3B cells were used to analyze changes in fluorescence anisotropy. Following trypsinization, 1×10^6 cells in 1 ml of PBS (10 mM, pH 7.4) were placed in quartz cuvettes. Next, 1,6-diphenyl-1,3,5-hexatriene (DPH) and 1-(4-(trimethyloamino)phenyl)-6-phenylhexa-1,3,5-triene (TMA-DPH) were added to the cells at final concentration of 2.5 μM and incubated for 30 min at 37 °C. The fluorescence anisotropy of DPH and TMA-DPH was measured using a PerkinElmer LS-50B spectrofluorometer (Waltham, Massachusetts, USA). Measurements were performed in PBS (10 mM, pH 7.4) at 37 °C. The excitation and emission wavelengths were set to 348 and 426 nm for DPH and 358 and 428 nm for TMA-DPH. Increasing concentrations of RB dissolved in HBSS (10 mM, pH 7.4) was added to the sample, and the anisotropy of fluorescence was measured again.

Fluorescence anisotropy was calculated using Perkin Elmer software and Jablonski's equation:

$$(1)\quad r = (I_{VV} - GI_{VH})/(I_{VV} + GI_{VH})$$

where r is fluorescence anisotropy, and I_{VV} and I_{VH} are the vertical and horizontal fluorescence intensities, respectively, to the vertical polarization of the excitation light beam. $G = I_{VH}/I_{VV}$ (grating correction factor) corrects the polarization effects of the monochromator.

2.6. Intracellular uptake inhibition assay

Cells were seeded into 24-well plates at a density of 1×10^5 cells/well and incubated for 24 h (37 ºC, 5% CO_2). The cells were subsequently pre-incubated with inhibitors (50 μM final concentration) for 1 h. Next, the cells were treated with RB (5 μM final concentration) for up to 3 h. Following incubation, the cells were washed with DPBS and detached using trypsin-EDTA solution. Following the addition of fresh culture medium, samples were gently mixed and collected for measurements. To estimate cellular uptake, fluorescence was measured using flow cytometry (LSRII, Becton Dickinson, Franklin Lakes, NJ, USA). The excitation and emission filters were 520 and 570 nm, respectively. The results are presented as the percentage of cells in the population that internalized RB.

2.7. Confocal microscopy

Caco-2, HT-29, HepG2, and Hep3B cells were seeded into black 96-well plates with a transparent glass bottom at a density of 1×10^4 cells/well followed by 24 h of incubation in standard conditions. The medium was replaced with 100 μL fresh culture medium containing RB (5 μM) and plates were incubated for 4 h in the dark (37 ºC, 5% CO_2). Cells were subsequently washed with DPBS and fixed with 4% formaldehyde solution for 15 min. Phalloidin–Atto 633 (1:400) was then added to each well for 20 min to stain F-actin in the cell membrane. Cells were washed with DPBS and 5 μM Hoechst 33342 was added to the cells for an additional 15 min to stain nuclear DNA. Following incubation, cells were washed with DPBS and submerged in 100 μL of fresh DPBS. Images were taken with a Leica TCS SP8 confocal microscope.

2.8. Cytotoxicity and phototoxicity studies

Caco-2, HepG2, Hep3B, and HT-29 cells were seeded into 96-well plates at a density of 1.5×10^4 cells/well. After 24 h of incubation (37 °C, 5% CO_2), 100 μL of fresh culture medium containing

different concentrations of RB was added to the cells and incubated for 5 h (37 ºC, 5% CO_2). The medium was then replaced with DPBS, and cells were irradiated for 30 min (2.4 J/cm^2/min) with the Q. Light Pro Unit lamp. Immediately after irradiation, DPBS was replaced with fresh culture medium, and cells were incubated for 24 h as a post-photodynamic therapy incubation. Additionally, the "dark" toxicity (without irradiation) and cytotoxicity of inhibitors were evaluated.

Cell viability was measured using the MTT assay. MTT was added to the wells (final concentration 0.5 mg/mL) and the plates were incubated for 2 h (37 ºC, 5% CO_2). After incubation, formazan crystals were dissolved in DMSO, and the absorbance was read at 570 nm using a PowerWave HT Microplate Spectrophotometer (BioTek, USA).

2.9. In silico analysis

Amino acid sequences were analyzed with Jalview software. Sequences obtained from the Protein Bank (NCBI) were used for the analysis. Tertiary protein structures were compared using the Swiss PDB viewer; the structures used for these comparisons were obtained from UniProt.

2.10. Western blot analysis

Cells were lysed in RIPA buffer (with PMSF and PIC) and the lysates were separated using SDS-PAGE electrophoresis and transferred to a nitrocellulose membrane (Amersham™ Protran®). After blocking with milk, the membrane was stained with primary antibodies (PA5106753- OATP1B1/1B3 (1:1000) and PA516914- beta-actin (1:10000) - Thermo Fisher Scientific, Waltham, MA, USA) at 4 °C overnight. After incubation, membranes were washed with PBS-Tween, and HRP-conjugated secondary antibodies were added (Goat anti-Rabbit IgG (H+L) Secondary Antibody, HRP (1:200000) Thermo Fisher Scientific, Waltham, MA, USA). Protein bands bound to HRP-conjugated secondary antibodies were visualized using the SuperSignal™ West Pico chemiluminescent substrate (Thermo Fisher Scientific, Waltham, MA, USA) and images were acquired with the ChemiDoc-IT2 (UVP, Meranco, Poznan, Poland). Beta-actin was used as the loading control.

2.11. Molecular Dynamics simulations

Molecular Dynamics (MD) simulations of lipid bilayers in the presence of RB molecules were carried out using GROMACS 2021.3 [11] and the CHARMM36 force field [12]. Graphical visualizations of molecular systems were assembled using the Visual Molecular Dynamics (VMD) software package [13]. The details of the computational methods are reported in Supplementary Information.

3. Results and discussion

As observed in previous studies of RB using spectroelectrochemical methodology (AC-modulated voltammetry involving fluorometric measurements) by Kakiuchi *et al.* [14,15], RB can undergo an interfacial ion transfer reaction with transient interfacial adsorption when doubly charged. The electrochemical 4-electrode cell used for the liquid-liquid interface polarization (see **Figure 1A** for cell scheme and employed electrodes configuration) supports a soft junction having around 1.4 cm in diameter. **Figure 1B** shows a series of cyclic voltammograms (CVs) of increasing RB concentrations (always initially added to the aqueous phase), starting from 10 µM. Observed signals at approx. -0.120 V (negative peak current corresponding to the transfer of the doubly charged RB anion from the

aqueous to the organic phase) and approx. -0.05 V (positive peak current corresponding to the transfer of the doubly charged RB anion from the organic to the aqueous phase) indicate that the electrochemically triggered ion transfer is reversible (the forward and reversed peak current ratio approaches unity). This was further confirmed by calibration curves plotted as **Figure 1C** where the negative and positive peak currents were plotted as a function of the RB aqueous phase concentration, which were linear over the studied concertation range (10–80 µM). This provides a voltammetric detection sensitivity (0.230 for positive and -0.252 $A \cdot M^{-1}$) with the expected order of magnitude, with similar absolute values expected for the revisable reaction [16,17]. Using the linear fit parameters, we additionally calculated the limit of detection and limit of quantification of RB for voltammetric detection at the electrified liquid-liquid interface. Obtained electroanalytical parameters are summarized in **Table 1**.

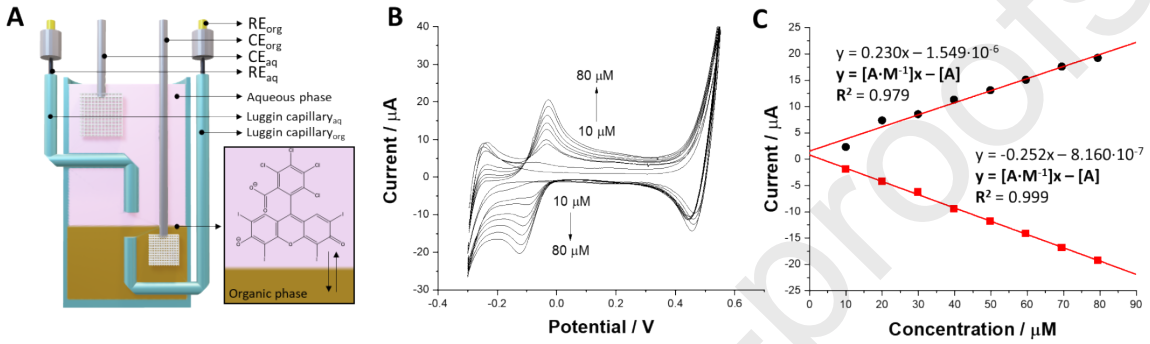

Figure 1. (A) The electrochemical cell used to study interfacial behavior of RB (RE: reference electrode, CE: counter electrode, aq: aqueous phase, org: organic phase). **(B)** CVs recorded for increasing concentrations of RB initially added to the aqueous phase. Concentrations ranged from 10 to 80 µM and the scan rate was 20 mV/s. **(C)** Calibration curves plotted based on the positive (-0.05 V) and negative (-0.12 V) peak current signals from CVs depicted in (B). Linear fit equations are: $y = 0.230x - 1.549 \cdot 10^{-6}$ [$y = [A \cdot M\text{-}1]x - [A]$], $R^2 = 0.979$ for positive signals and $y = -0.252x - 8.160 \cdot 10^{-7}$ [$y = [A \cdot M\text{-}1]x - [A]$], $R^2 = 0.999$ for negative signals.

The carboxylic group and phenolic site present within the xanthene-based moiety of the RB chemical structure are the acid-base centers responsible for molecule ionization. At acidic pK_a values, pK_{a1} = 1.89 and pK_{a2} = 3.93 [18], RB is expected to be negatively charged within the full conventional pH scale, which is further depicted on a concentration fraction diagram in **Figure 2A**. At pH < 1, the non-dissociated RB (RB^0) fraction predominates; as the pH increases, the concentration of monoanionic RB (RB^-) species reaches its maximum value with a concentration fraction slightly exceeding 80% at pH 2.9. Further aqueous phase alkalization changes the RB speciation. At pK_{a2}, the concertation of monoanionic RB is equal to the concentration of doubly anionic species (RB^{2-}). From approximately pH 6.3 onwards, only doubly charged RB species are expected to be present in the bulk of the aqueous phase. Thus, the aqueous phase was fixed at pH 7 to perform the scan rate dependency allowing the calculation of the diffusion of interfacially active species (**Figure 2B and 2C**)**.** Using the Randles-Sevcik equation, which is valid for reversible ion transfer reactions, the aqueous phase diffusion coefficient was calculated as 1.55 ± 0.60 cm^2/s (experiment performed in triplicate).

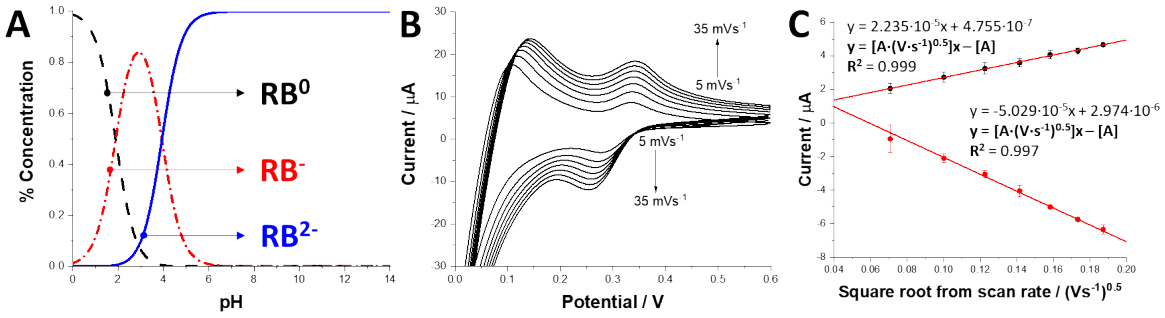

Figure 2. (**A**) Concentration fraction diagram plotted for RB using pK_{a1} = 1.89 and pK_{a2} = 3.93. (**B**) CVs recorded in the presence of 50 µM RB in the aqueous phase at pH = 7.0 (RB^{2-}) and at different scan rate values (5, 10, 15, 20, 25, 30, and 35 mV/s). (**C**) Ionic current values for the interfacial transfer of RB plotted as the square root of the scan rate. The linear fit equation is given next to the corresponding dependencies. Linear fit equations are: $y = 2.235 \cdot 10^{-5}x + 4.755 \cdot 10^{-7}$ [$y = [A \cdot (V \cdot s^{-1})^{0.5}]x - [A]$], $R^2 = 0.999$ for positive signals and $y = -5.029 \cdot 10^{-5}x - 2.974 \cdot 10^{-6}$ [$y = [A \cdot (V \cdot s^{-1})^{0.5}]x - [A]$], $R^2 = 0.997$ for negative signals.

Table 1. Summary of electroanalytical, physicochemical, and pharmacochemical parameters extracted from the voltammetric study.

Parameter (unit)	Value	Parameter (unit)	Value
Sensitivity[1] (+) ($A \cdot M^{-1}$)	0.230	$\Delta^{aq}_{org}\phi'$ (V)	-0.095
Sensitivity[1] (-) ($A \cdot M^{-1}$)	0.252	$\Delta^{aq}_{org}G'^{4}$ ($kJ \cdot mol^{-1}$)	21.8
LOD[2] (+) (µM)	8.91	$logP_{DCE}$[5]	3.26
LOD[2] (-) (µM)	2.18	D[6] (+) ($cm^2 \cdot s^{-1}$)	0.35 ± 0.07
LOQ[3] (+) (µM)	29.70	D[6] (-) ($cm^2 \cdot s^{-1}$)	1.55 ± 0.60
LOQ[3] (-) (µM)	7.26	z[7] (pH = 7)	-2

[1]Taken as the slope of the calibration curve plotted as the ion transfer current vs the corresponding concentration. [2]Calculated using the limits of detection (LOD) = $3SD \cdot S^{-1}$ where SD is the standard deviation of the calibration curve intercept and S is the slope (sensitivity value). [3]Calculated using the LOD = $10SD \cdot S^{-1}$. [4]Free Gibbs energy of ion transfer reaction is given as $\Delta^{aq}_{org}G' = -\Delta^{aq}_{org}\phi' \cdot z \cdot F$. [5]Calculated using $logP_{DCE} = -(\Delta^{aq}_{org}\phi' \cdot z \cdot F) \cdot (2.303 \cdot R \cdot T)^{-1}$ where F is the Faraday constant, R is the gas constant, and T is the temperature in K. [6]Calculated using the Randles-Sevcik equation; the error was derived from three independent experiments. [7]Charge was derived from the concertation fraction diagram.

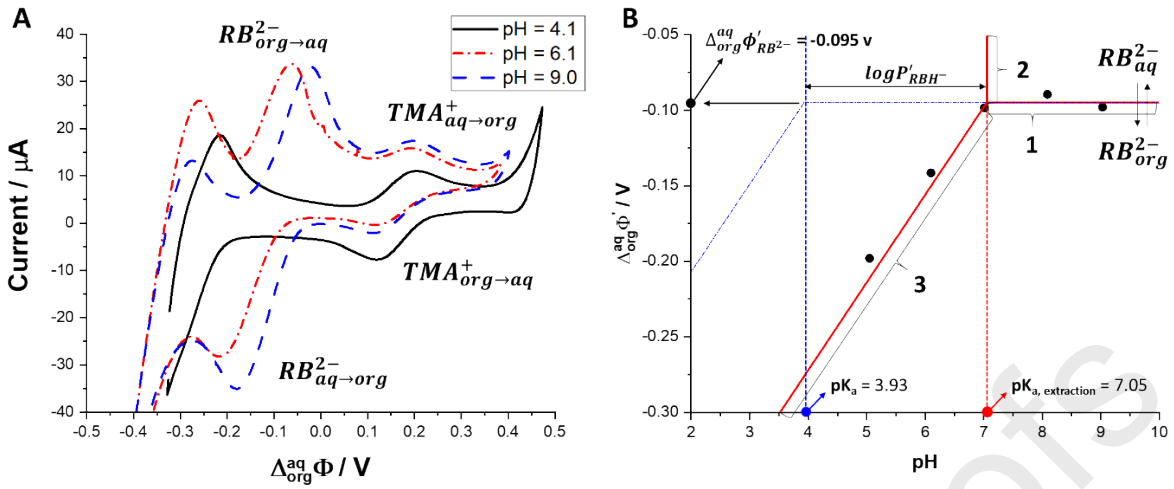

Figure 3. (A) CVs recorded in the presence of 100 µM RB and 50 µM TMA^+Cl^- in the aqueous phase at three different aqueous phase pH values, which were as follows: 4.09 (solid black line), 6.1 (dash-dot red line), and 9.0 (dashed blue line). **(B)** Ionic partition diagram for double anionic RB. The boundary lines affected by the RB extraction pK_a are marked with the solid red line. The theoretical ionic portion diagram for RB is marked with the dotted blue lines. For more details, see the discussion section [19–22].

Finally, the CVs recorded at different pH values (**Figure 3A**; pH = 4.1, 6.1, and 9.0) were used to plot the ion partition diagram (**Figure 3B**). Here, solid red lines correspond to the equivalent concentration boundary lines that were plotted using equations developed in [19].

Boundary line 1 corresponds to a situation where the concentration of RB^{2-} in the aqueous phase is equal to the concentration of RB^{2-} in the organic phase:

$$\Delta^{aq}_{org}\phi = \Delta^{aq}_{org}\phi'_{RB^{2-}} - \frac{2.3RT}{F}\left(logP'_{RB^-} + pK_a^{aq}\right) + \frac{2.3RT}{F}pH \quad (2)$$

Boundary line 2 describes a scenario where the aqueous concentration of RB^{2-} is equal to the organic phase concentration of RB^- and is given by:

$$\Delta^{aq}_{org}\phi = \Delta^{aq}_{org}\phi'_{RB^{2-}} - \frac{2.3RT}{F}\left(logP'_{RB^-} + pK_a^{aq}\right) + \frac{2.3RT}{F}pH \quad (3)$$

Finally, boundary line 3 (proton involved ion transfer reaction facilitated by the monoanionic form of RB in the organic phase) is predicted with the following equation:

$$\Delta^{aq}_{org}\phi = \Delta^{aq}_{org}\phi'_{RB^{2-}} - \frac{2.3RT}{F}\left(logP'_{RB^-} + pK_a^{aq}\right) + \frac{2.3RT}{F}pH \quad (4)$$

The presence of RB in the aqueous phase lies above boundary line 1, corresponding to a potential difference of -0.095 V. As the pH decreases from 7 toward pK_a = 3.93, the fraction of doubly charged RB species decreases and the $\Delta^{aq}_{org}\phi'$ shifts toward more negative potential values, finally giving a signal (**Figure 3A**, black solid line recorded at pH 4.1) that is partly overlaid with the potential window limiting ion transfer. Since complex splitting voltammetric signals expected for chemical species with more than one ionizable functional group were not observed, we concluded that the points marked within boundary line 3 (**Figure 3B**) were due to the facilitated transfer of protons by the monoanionic RB species, which may partition to the organic phase (the logP_{DCE} for RB^- is expected to be lower than 3.26 calculated for RB^{2-}), and are overlaid with the simple RB^{2-} ion transfer reaction.

From the ion partition diagram, the extraction p*K*a value, defined as the apparent p*K*a of RB^- dissolved in the organic phase, was found to be approximately 7.05. Therefore, we can conclude that the interfacial transfer of RB follows a simple ion transfer reaction. The $logP_{DCE}$ value indicates that RB displays moderate hydrophobicity; thus, its affinity for the hydrophobic domains of the lipidic membrane cannot be neglected.

To further investigate the interactions of RB with membrane models, we first analyzed the interactions of RB with negatively charged micelles comprised of LPS using DLS measurements. Changes in the size or disruption of LPS micelles were used as a measure of RB-membrane interactions. LPS-based soft objects were visible as two distribution peaks (a smaller peak at 20 nm and a bigger peak at 140 nm (**Figure S1**)), with the latter attributed to LPS micelles [23]. The addition of RB up to 50 μM did not change the sizes of the distribution curves; however, further increases in the RB concentration (100 μM and 200 μM) changed the sizes of the distribution curves, revealing a smaller sized peak. This change suggests that RB addition dissociated the LPS micelles and that a threshold concentration of RB must be exceeded to change the size of negatively charged micelles. However, it should be emphasized that the concentrations of RB used for this analysis are significantly higher than the concentrations used in our previous cytotoxicity studies [3,6].

Next, using fluorescence anisotropy measurements of two fluorescent probes (DPH and TMA-DPH), we measured changes in membrane fluidity in various layers of the cell membrane. DPH binds to the hydrophobic part and TMA-DPH binds to hydrophilic part of the bilayer [24]. The subsequent addition of RB resulted in an increase in only TMA-DPH fluorescence anisotropy, indicating stiffening of the cellular membrane due to the interaction of RB with the hydrophilic part of the membrane (**Figure 4A and B**). Here it should be noted here that the limitation of the method did not allow the study of the impact of higher concentrations of RB. These results suggest that RB does not possesses the ability to diffuse into deeper layers of the cellular membrane.

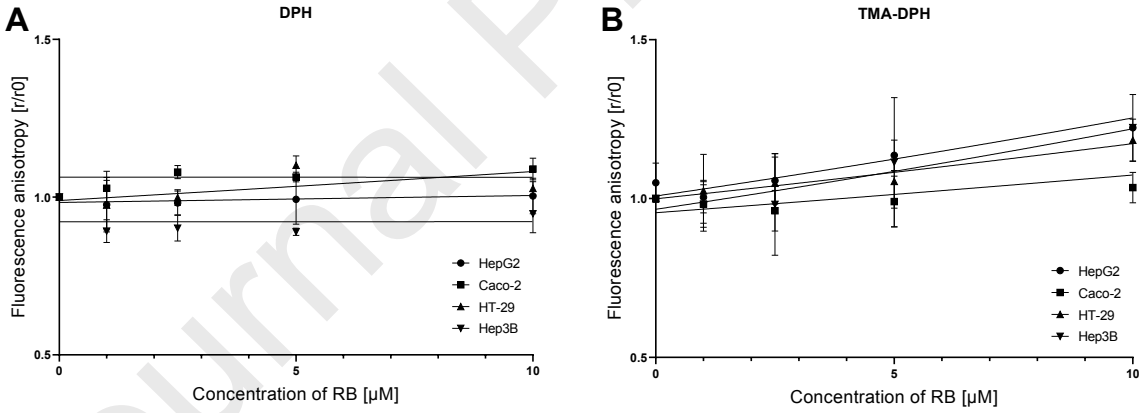

Figure 4. Changes in fluorescence anisotropy of **(A)** DPH and **(B)** TMA-DPH incorporated in the membranes of HepG2, Hep3B, HT-29, and Caco-2 cells with increasing concentrations of RB (0.5 to 10 μM in PBS, pH 7.4, 37 °C).

RB molecules carry two ionizable groups (-OH and -COOH) that are predominantly found in the deprotonated form (indicated as O^- and CO_2^-, respectively) at physiological pH values. This consideration, together with the DPH and TMA-DPH results, led us to hypothesize that RB might interact with the positive surface charge of lipid membranes through electrostatic interactions, without being able to penetrate spontaneously inside the lipid phase.

Thus, we next used all-atom MD simulations to obtain additional insights into how RB interacts with lipid bilayers at the molecular level. MD simulations with a mammalian phospholipid bilayer model,

representative of the cell membrane, in the presence of RB molecules in the surrounding aqueous solvent, revealed a strong interaction between RB and hydrophilic lipid heads. After an initial equilibration phase, RB rapidly formed stable interactions with the membrane outer surface (**Figure 5A and B**); no subsequent spontaneous permeation events were observed at either low (1 RB molecule) or high (10 RB molecules) RB concentrations throughout the 1 μs MD sampling time period (see **Supplementary Video 1 and 2**).

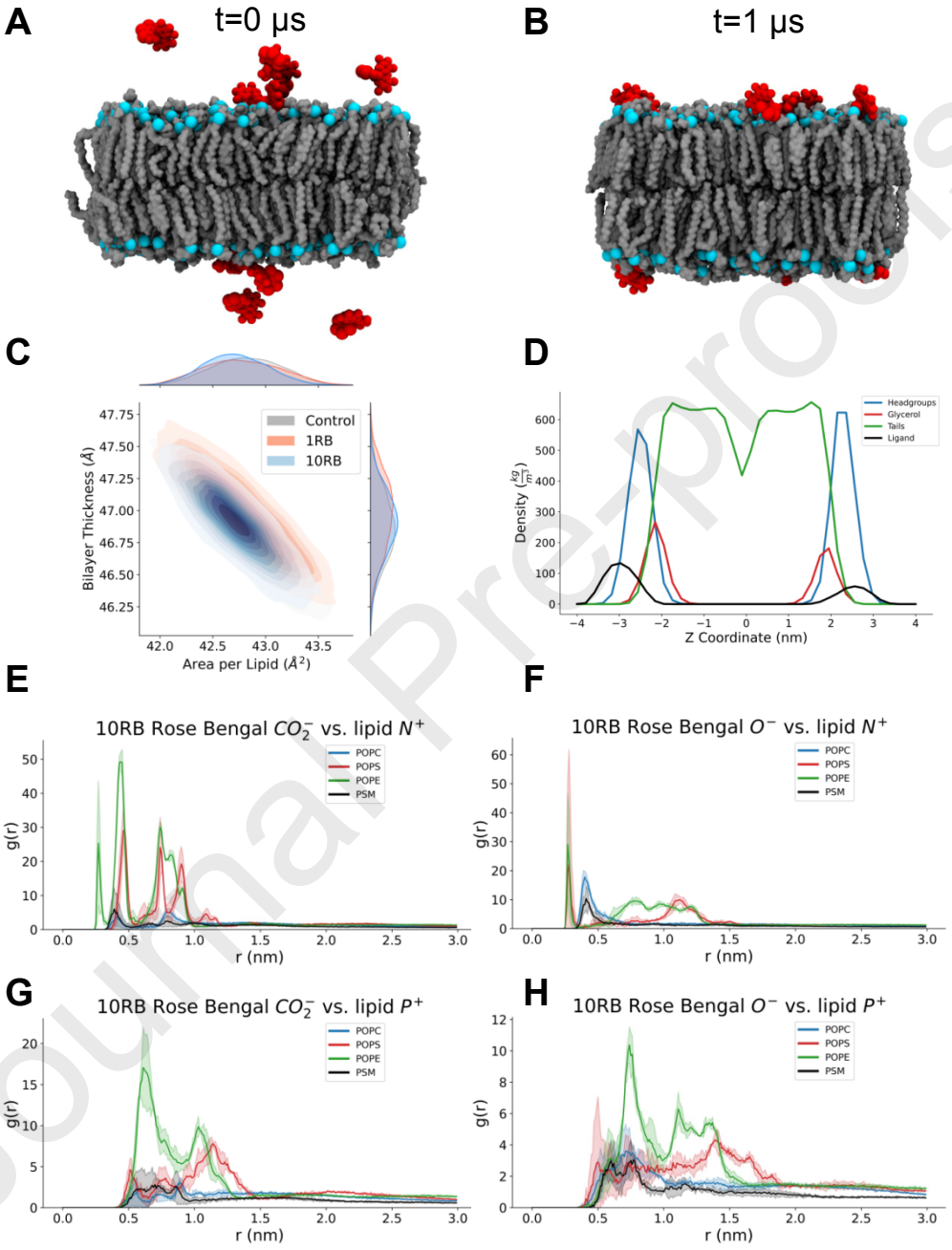

Figure 5. Results of MD simulations of the lipid bilayer with rose bengal. **(A)** Snapshot of the initial conditions of the MD simulation with 10 RB molecules (in red), with ligands dispersed in the solvent. **(B)** Snapshot of the same MD trajectory with 10 RB molecules at the end (t = 1 μs) of the simulation, showing the system had reached equilibrium. Lipids are shown in gray, with phosphorus headgroups highlighted in cyan. **(C)** The distributions of the gAPL (x axis) and bilayer thickness (y axis) in the control simulation (gray), at low RB concentration (red), and at high RB concentration (blue) are shown. Marginal axes show the individual distributions. **(D)** Density profiles of lipid headgroups

(blue), glycerol groups (red), acyl chains (green), and RB (black) in the high-concentration simulation (10 RB). The plot is centered at the bilayer core, where z = 0. **(E-H)** Radial distribution functions highlighting the distances between RB CO_2^- groups and lipid head nitrogen atoms **(E)** and phosphorus **(G)** atoms, in addition to the distances between RB O^- groups and lipid head nitrogen **(F)** and phosphorus **(H)** atoms. Shaded intervals in panels **(E-H)** represent 95% confidence intervals calculated from block averaging.

The analysis of the geometrical parameters of the membrane, i.e., the membrane thickness (δ) and the geometric area per lipid (gAPL), provided an initial assessment of both the quality of the simulated bilayer and of the effects of RB on membrane structure (**Figure 5C**). Indeed, the gAPL is a parameter that is directly linked to the molecular order and diffusion pattern of the lipids, and together with the membrane thickness constitutes a quantitative measurement of the equilibrium of the simulations. As shown in **Table 2**, the control simulation without RB yielded an average gAPL value of 42.82 $Å^2$ (95% CI: 42.67 – 42.97) and an average thickness value of 46.87 Å (95% CI: 46.76 – 46.98). These values are consistent both with earlier simulations using the same membrane model [25–27] and with experimental data describing lipid bilayers with a comparable cholesterol content (approximately 34%) [28], thus confirming the convergence of the bilayer simulation.

Table 2. gAPL and bilayer thickness calculated from the MD simulations (95% CIs are reported in square brackets).

System	gAPL ($Å^2$)	Bilayer Thickness (δ) (Å)
Control	42.82 [42.67 – 42.97]	46.87 [46.76 – 46.98]
1 RB	42.78 [42.66 – 42.90]	46.98 [46.88 – 47.08]
10 RB	42.72 [42.56 – 42.88]	46.90 [46.78 – 47.02]

The addition of up to 10 RB molecules in the simulation box, in random initial positions in the aqueous solvent, resulted in no remarkable effect on membrane geometry in terms of gAPL and thickness, which is consistent with the lack of membrane permeation events (**Figure 5C**).

The density profile analysis of different membrane components in the presence of RB with respect to the z axis provides additional information regarding membrane geometry and the exact localization of RB. As shown in **Figure 5D** and **Supplementary Figure S7**, the addition of RB in the simulations did not alter the overall density profiles of the different lipid groups, and the position of the density peaks of RB molecules confirmed that they were localized in close proximity to lipid headgroups in the aqueous phase throughout the simulation.

Furthermore, the effects of RB on the overall mobility of the lipid chains and lipid packing were analyzed using deuterium order parameters, S_{CD}. The control simulation results were in good agreement with previously published MD simulation results of membranes with similar lipid compositions [29], confirming the quality of the membrane model and highlighting the ordering effect

induced by cholesterol in lipid bilayers. As shown in **Supplementary Figure S7**, the addition of RB and its interaction with the membrane surface did not significantly alter lipid order parameters, which remained comparable, within error, to those of the control simulation at both low and high RB concentrations.

Overall, MD simulations of RB with the lipid bilayer suggest no remarkable effect of RB on bilayer geometry and packing, both at low (1 RB) and high (10 RB) concentrations. The exact nature of the interaction of RB with the polar headgroups of lipids was investigated by calculating radial distribution functions (RDFs) between the ionized groups of RB, i.e., the deprotonated CO_2^- and O^- groups, and the positively charged P^+ and N^+ atoms on the lipid heads. The RDF is related to the probability of finding two given atom groups at a given distance with respect to each other. The results suggest a strong interaction of the deprotonated groups of RB with positively charged amine groups in the lipid heads (**Figure 5E and F**), as highlighted by the presence of substantial RDF peaks below 5 Å for both CO_2^- and O^- of RB with respect to the lipid N^+ species. Conversely, peaks were localized at slightly higher distances (between 5 and 15 Å) when calculated with respect to lipid P^+ atoms (**Figure 5G and H**). The corresponding results for the simulation at low RB concentration (**Supplementary Figure S8**) revealed the same overall trend, with RB ionized groups in close proximity to lipid head N^+ atoms. These results suggest that the largely deprotonated CO_2^- and O^- groups of RB at physiological pH values rapidly form an electrostatic interaction with the membrane surface, maintaining the anchoring of RB to the bilayer and hindering its penetration into the hydrophobic membrane core. To further explore this hypothesis, we quantified the strength of the interactions between the RB molecule and the lipid headgroups using the MM/PBSA approach. RB interacts with the solvent-exposed portion of the lipid bilayer with a predicted total free energy of -75.54 kcal/mol [95% CI: -80.04 to -71.05 kcal/mol], which is of the same order of magnitude of previously reported predictions of RB-protein binding [30]. While the aim of this method is not to accurately quantify the energy barrier preventing the RB from penetrating the bilayer (e.g. due to the lack of the entropic contribution), the negative binding free energy values that were obtained, resulting from the overall interactions between RB and the lipid headgroups, are about 10-fold above the thermal noise level (0.6 kcal/mol at room temperature) and thus indicative of its resistance to spontaneous membrane crossing, caused by strong electrostatic effects between the charged groups of the ligand and the hydrophilic portion of the membrane. Indeed, the results obtained from the MD simulations are consistent with the those obtained with the DPH and TMA-DPH probes, which suggested close proximity of RB to the hydrophilic part of the lipid bilayer, with a negligible interaction with the aliphatic core and no membrane permeation.

The cell lines used in the fluorescence anisotropy experiments were selected for further experiments to evaluate the cellular uptake of RB. These four cell lines, derived from colorectal cancer and hepatocellular carcinoma, express high levels of OATP transporters [9]. We showed that cellular uptake of RB was significantly higher in hepatocellular carcinoma cell lines (HepG2 and Hep3B) than in colorectal cancer cell lines (Caco-2 and HT-29) (**Figure 6A**). It is noteworthy that Caco-2 and HT-29 cells did not internalize RB over the entire time range, while almost 40% and 60% of HepG2 and Hep3B cells, respectively, internalized RB. These findings were supported by confocal microscopy images showing RB inside both HepG2 and Hep3B RB cells and not inside Caco-2 or HT-29 cells (**Figure 6B and Figure S3**).

RB is a commonly known photosensitizing agent in photodynamic therapy. In this therapy, the combination of RB, a light source, and oxygen leads to the generation of singlet oxygen species and free radicals, which are cytotoxic to tumor cells [1]. Therefore, we assessed the cytotoxic effect of RB in all tested cell lines following irradiation by light with an appropriate wavelength (**Figure 6C**). The highest cytotoxic effect was observed for HepG2 and Hep3B cells, for which the RB IC_{50} values were 5.03 and 2.75 μM, respectively. On the other hand, the RB IC_{50} values for Caco-2 and HT-29 cell lines were 4- to 5-fold higher **(Table S4)**. Dark toxicity was not observed. Therefore, we can conclude that the significant difference in intracellular uptake of RB between hepatocellular carcinoma and colorectal cancer cell lines translated into differences in the cytotoxicity of RB between these cells.

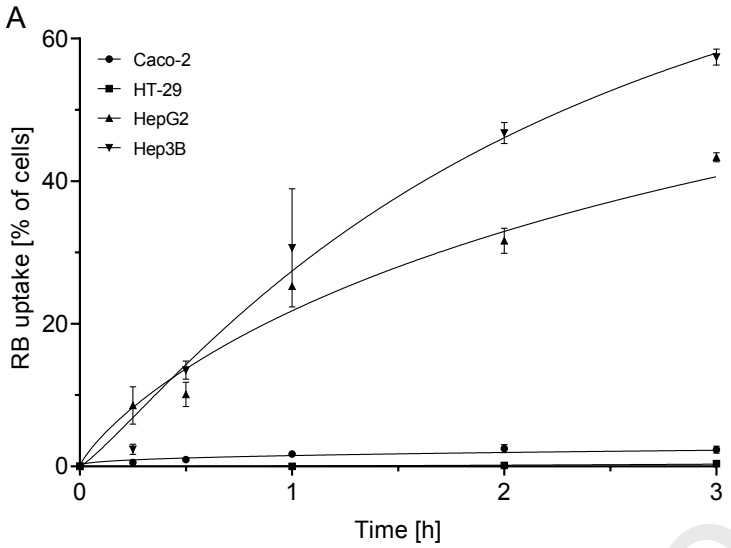

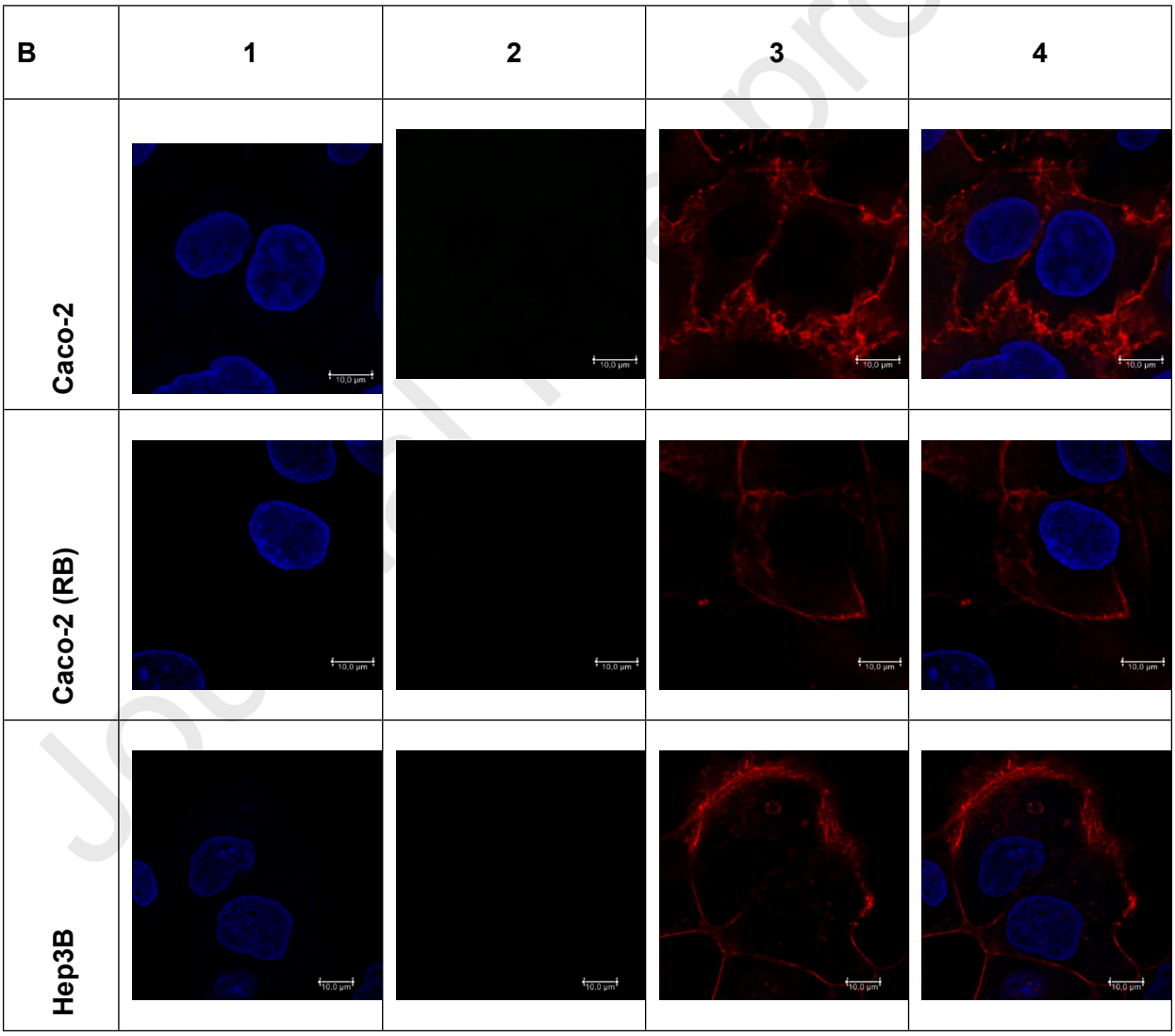

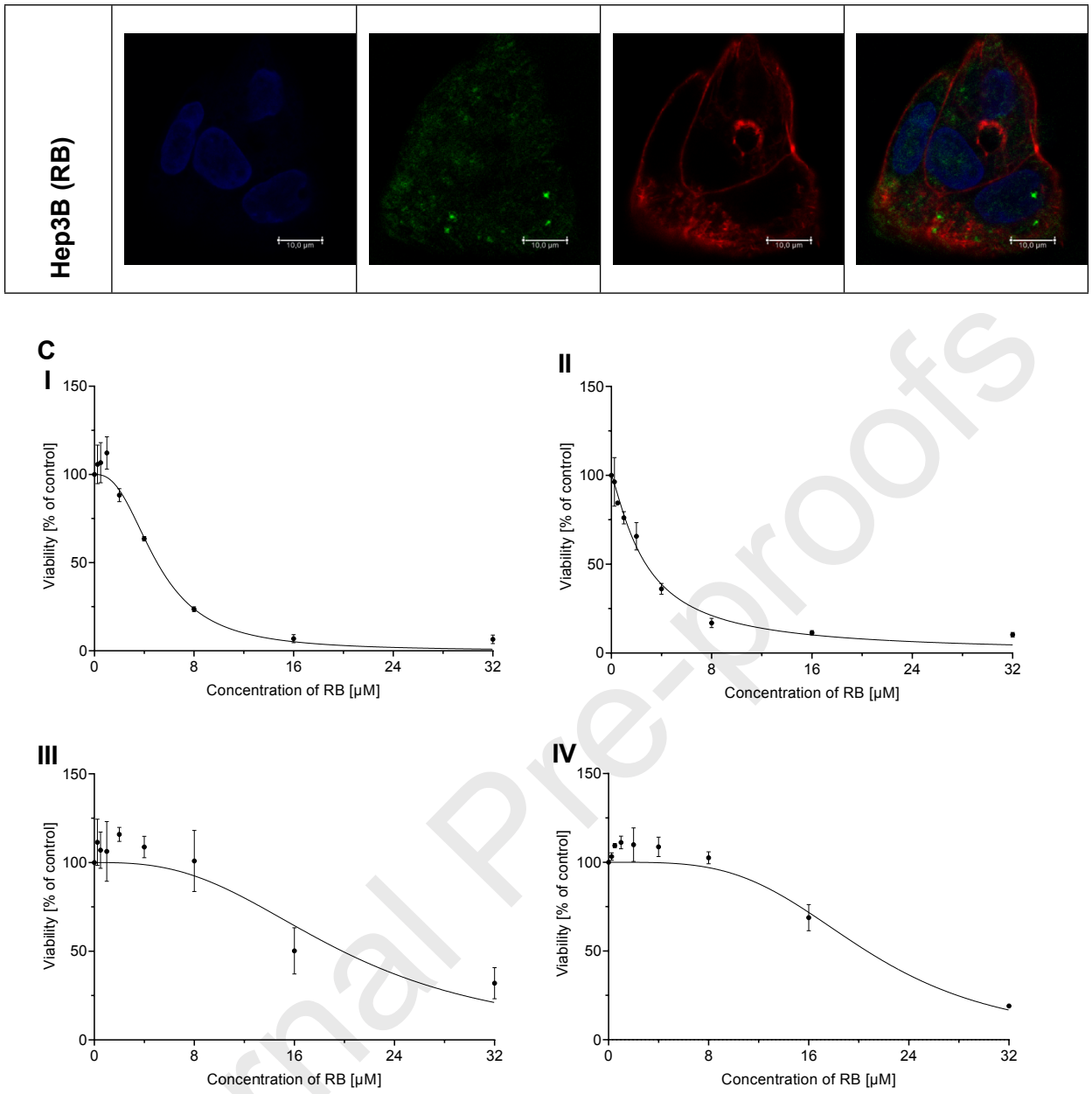

Figure 6. (A) Cellular uptake of RB (5 μM) by Caco-2, HT-29, HepG2, and Hep3B cell lines. **(B)** Confocal micrographs of Caco-2 and HepG2 cell lines: (1) Hoechst 33342 (nucleus, blue), (2) RB (green), (3) Phalloidin–Atto 633 (F-actin, red), and (4) merging of channels 1, 2, and 3. The scale bar represents 10 μm. **(C)** Phototoxic effect of RB in (I) HepG2, (II) Hep3B, (III) Caco-2, and (IV) HT-29 cells. Cell viability was determined using the MTT assay. Data are presented as percentages of the viability of control (untreated) cells; means ± SD; n = 3.

Together with the results of previous research, our observations suggest that differences in the uptake and cytotoxicity of RB by these cells might be due to differences in their expression of OATPs, which play roles in the cellular influx and efflux of compounds and renal drug excretion [31], and mediate cellular uptake of compounds such as fluorescein and its derivatives [9,32]. To determine the potential role of OATPs in RB uptake in hepatocytes, we used specific, well-described inhibitors of OATP family transporters [33–35]. These inhibitors significantly reduced intracellular accumulation of RB, especially in HepG2 cells (**Figure 7**). While the baseline number of HepG2 cells internalizing RB was

approximately 40% after 3 h of incubation, inhibitors reduced the number of RB-positive cells to less than 10%, clearly indicating the significant role of OATPs transporters in RB internalization.

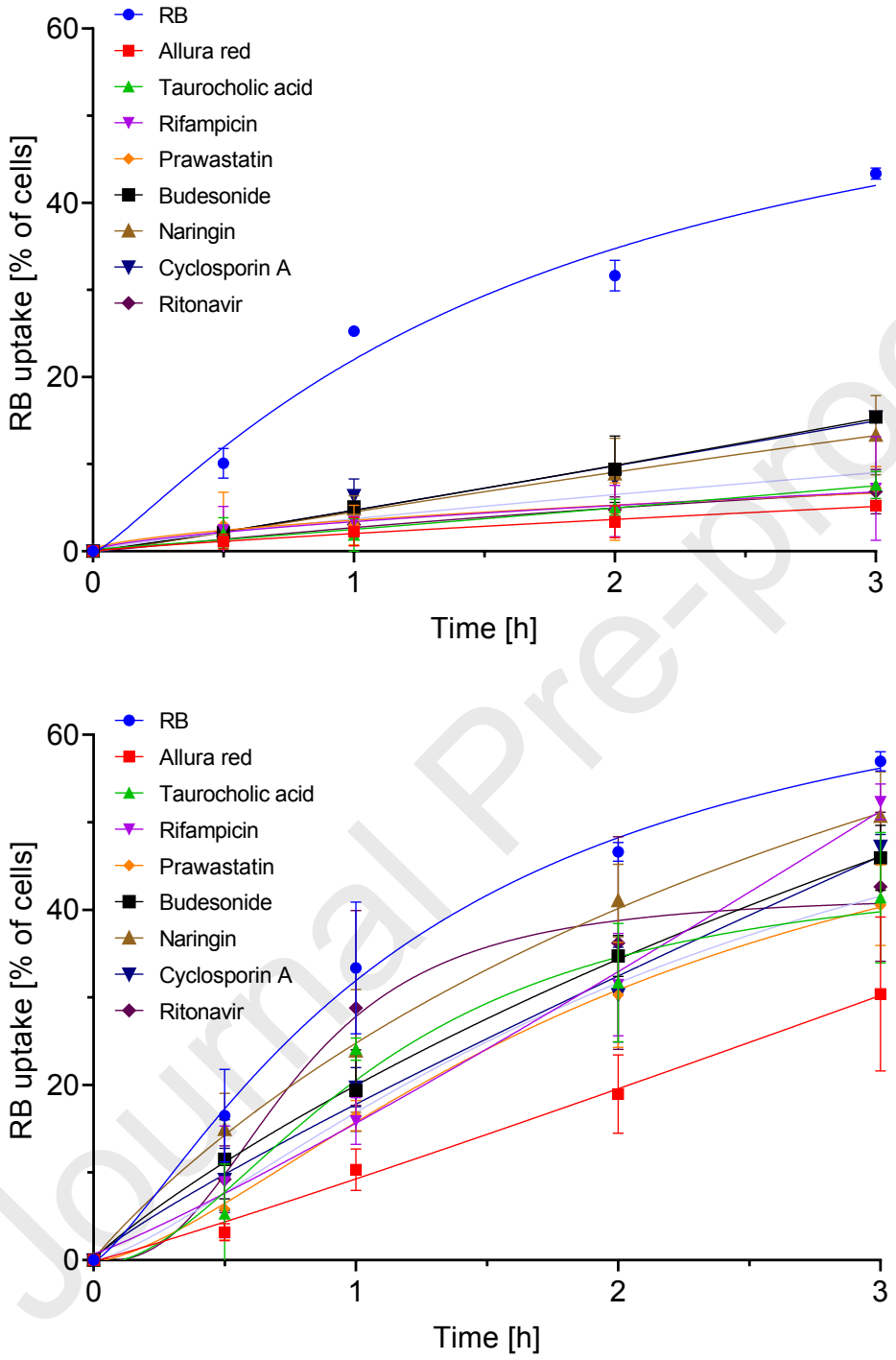

Figure 7. Uptake of RB in **(A)** HepG2 and **(B)** Hep3B cells after treatment with OATP inhibitors, evaluated using flow cytometry. Data are presented as mean ± SD, n = 3. A statistically significant difference ($p < 0.05$) in RB uptake between nontreated cells and cell pretreated with each inhibitor is presented in SI (**Table S4**).

Selected inhibitors, which alone had no impact on cell viability (**Figure S3**), decreased the phototoxic effect of RB in HepG2 and Hep3B cell lines (**Figure 8**). This effect was especially visible in HepG2 cells, which showed higher susceptibility to OATP inhibitors in uptake assays.

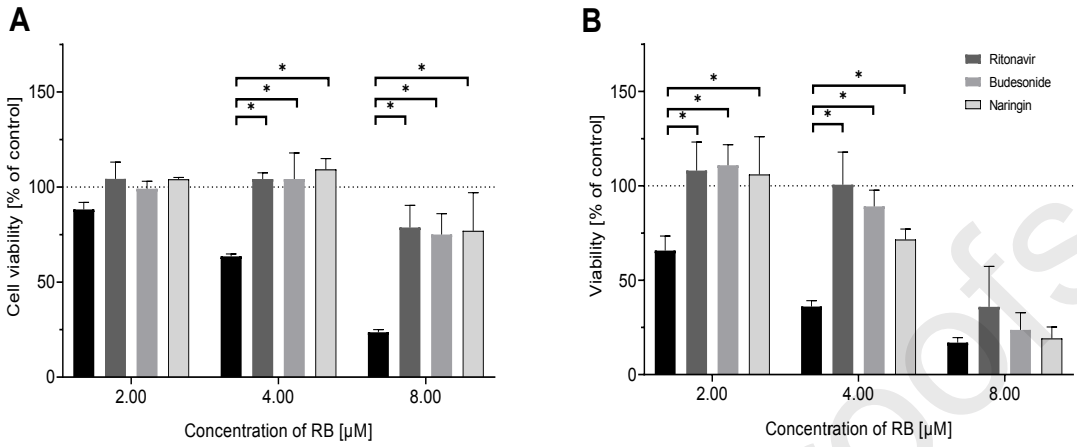

Figure 8. Phototoxic effect of RB in **(A)** HepG2 and **(B)** Hep3B cells after treatment with selected OATP inhibitors. Cell viability was determined using the MTT assay. Data are presented as percentages of the viability of the control (untreated) cells; mean ± SD, n = 3.

The main difference between the colorectal cancer and hepatocellular carcinoma cell lines in terms of OATPs is that OATP1B1 and OATP1B3 transporters are expressed abundantly in HepG2 and Hep3B cells, but not in Caco-2 or HT-29 cells [36]. OATP1B1 is also more frequently found in the liver, as shown by the significantly higher level of OATP1B1 mRNA compared with OATP1B3 mRNA [36]. However, despite this difference, OATP1B1 and OATP1B3 are very similar in DNA sequence, amino acid sequence, and tertiary structure [10]. Sequence alignment showed that both transporters share 79.91% amino acid identity (**Figure S4C**), and the epitope recognized by the antibody used in our Western blot analysis only differs in three amino acids between OATP1B1 and OATP1B3 (**Figure S6**). Therefore, it may not be possible to distinguish between these two proteins using this antibody, as reported previously [37]. However, Western blotting can still be used to determine whether there are differences in the expression of either of these two transporters in the cells studied, at the same time being responsible for differences in RB transport. Indeed, the expression of OATP1B1/1B3 was significantly higher in hepatocellular carcinoma cell lines than in colorectal cancer cell lines (**Figure 9**). Together, our data indicate that OATP1B1/1B3 are crucial for cellular uptake of RB.

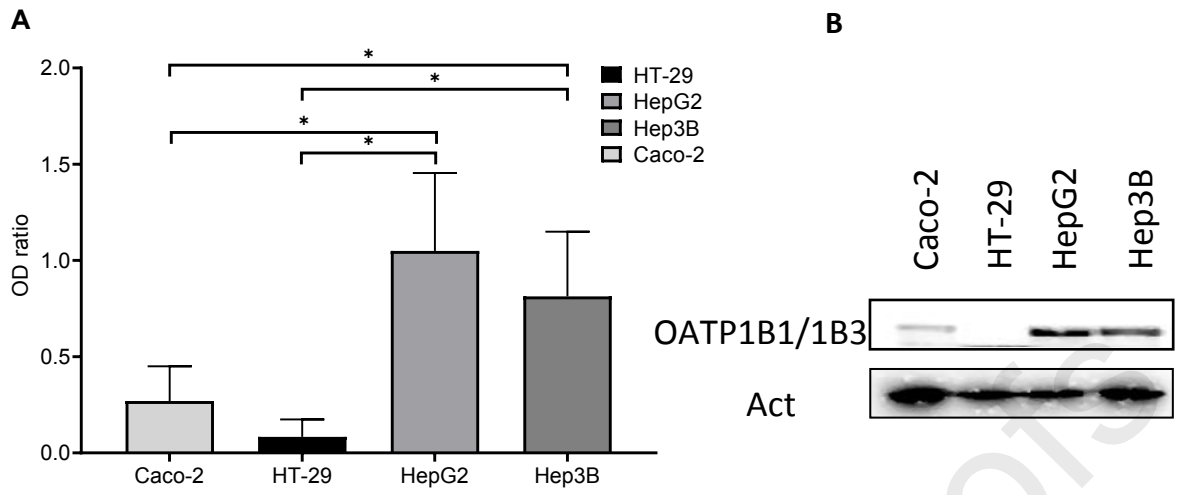

Figure 9. (A) Densitometric analysis of protein bands on Western blots. Each bar represents the mean optical density of each band from four independent experiments normalized to that of the beta-actin band. **(B)** Representative image of OATP1B1/1B3 content in cell lysates evaluated by Western blotting. Beta-actin was used as a loading control.

4. Conclusions

RB is a promising photosensitizer for anticancer photodynamic therapy. Previous and current scientific efforts have focused on using nanocarriers to transport this photosensitizer inside cells, since the success of RB treatment depends on its cellular uptake and intracellular accumulation. Interestingly, the mechanism of cellular entry of RB has remained unclear. In the present study, electrochemical studies performed at the junction between two immiscible electrolyte solutions, as well as model DLS and fluorescence polarization assays, showed that RB displays moderate-to-no interactions with hydrophobic domains of the lipid bilayers. We anticipate, that proposed electrified soft junction, along with other electrochemical platforms mimicking the bio-membranes (e.g. black lipid bilayers) can be further used to study the diffusivity of RB alone or as a complex formed with the OATP

These observations were strengthened by molecular modeling, showing that RB can interact with the membrane surface, but cannot cross cellular membranes by itself, indicating the necessity for membrane protein transporters. *In vitro* experiments showed a significant difference in intracellular uptake and phototoxicity between hepatocellular carcinoma and colorectal cancer cell lines, which differ in their expression of OATP transporter family proteins. Further studies using specific inhibitors of OATP transporters revealed their crucial role in transporting RB into cells. The results reveal the previously unknown importance of OATP transporters in facilitating RB uptake, which could have implications for photodynamic therapy with RB and lead to the development of effective RB delivery systems.

CEediT

Krzysztof Sztandera: methodology, formal analysis, investigation, writing – original draft, writing - review & editing, visualization

Michał Gorzkiewicz: conceptualization, methodology, investigation, writing – original draft, writing - review & editing, visualization

Eric A. Zizzi: methodology, investigation, writing – original draft, writing - review & editing, visualization

Natalia Dybczak: investigation

Lukasz Poltorak: data curation, writing -review & editing, supervision

Marco A. Deriu: writing - review & editing, supervision

Barbara Klajnert-Maculewicz: writing - review & editing, supervison, project administration, funding acquisition

Acknowledgements

This work was supported by the National Science Centre, Poland (Project UMO-2017/25/B/NZ7/01304 ″Phosphorus dendrimers as carriers for photosensitizers - in vivo studies″) and based upon work from COST Action ″Nano2Clinic. Cancer Nanomedicine - from the bench to the bedside″ CA17140 supported by COST (European Cooperation in Science and Technology). L.P. is grateful to the National Science Centre, Poland (Project UMO-2021/43/O/ST4/01553).

References

[1] K. Sztandera, M. Gorzkiewicz, B. Klajnert-Maculewicz, Nanocarriers in photodynamic therapy—in vitro and in vivo studies, Wiley Interdiscip. Rev. Nanomedicine Nanobiotechnology. 12 (2020) 1–24.

[2] S. Demartis, A. Obinu, E. Gavini, P. Giunchedi, G. Rassu, Nanotechnology-based rose Bengal: A broad-spectrum biomedical tool, Dye. Pigment. 188 (2021) 109236. https://doi.org/10.1016/j.dyepig.2021.109236.

[3] K. Sztandera, M. Gorzkiewicz, X. Wang, S. Boye, D. Appelhans, B. Klajnert-Maculewicz, pH-stable polymersome as nanocarrier for post-loaded rose bengal in photodynamic therapy, Colloids Surfaces B Biointerfaces. 217 (2022) 112662.

[4] K. Sztandera, M. Gorzkiewicz, M. Bątal, V. Arkhipova, N. Knauer, J. Sánchez-Nieves, F.J. de la Mata, R. Gómez, E. Apartsin, B. Klajnert-Maculewicz, Triazine–Carbosilane Dendrimersomes Enhance Cellular Uptake and Phototoxic Activity of Rose Bengal in Basal Cell Skin Carcinoma Cells, Int. J. Nanomedicine. 17 (2022) 1139–1154.

[5] M. Dabrzalska, A. Janaszewska, M. Zablocka, S. Mignani, J.P. Majoral, B. Klajnert-Maculewicz, Cationic Phosphorus Dendrimer Enhances Photodynamic Activity of Rose Bengal against Basal Cell Carcinoma Cell Lines, Mol. Pharm. 14 (2017) 1821–1830.

[6] K. Sztandera, M. Gorzkiewicz, A.S. Dias Martins, L. Pallante, E.A. Zizzi, M. Miceli, M. Bątal, C.P. Reis, M.A. Deriu, B. Klajnert-Maculewicz, Noncovalent Interactions with PAMAM and PPI Dendrimers Promote the Cellular Uptake and Photodynamic Activity of Rose Bengal: The Role of the Dendrimer Structure, J. Med. Chem. 64 (2021) 15758–15771.

[7] S.T.G. Buck, F. Bettanin, E. Orestes, P. Homem-De-Mello, H. Imasato, R.B. Viana, J.R. Perussi, A.B.F. Da Silva, Photodynamic Efficiency of Xanthene Dyes and Their Phototoxicity against a Carcinoma Cell Line: A Computational and Experimental Study, J. Chem. 2017 (2017).

[8] B. Alberts, A. Johnson, J. Lewis, M. Raff, K. Roberts, P. And Walter, Principles of Membrane Transport, in: Mol. Biol. Cell, 2007: p. 1392. https://www.ncbi.nlm.nih.gov/books/NBK26815/ (accessed August 1, 2022).

[9] M. Roth, A. Obaidat, B. Hagenbuch, OATPs, OATs and OCTs: The organic anion and cation transporters of the SLCO and SLC22A gene superfamilies, Br. J. Pharmacol. 165 (2012) 1260–1287.

[10] A. Tuerkova, O. Ungvári, R. Laczkó-Rigó, E. Mernyák, G. Szakács, C. Özvegy-Laczka, B. Zdrazil, Data-Driven Ensemble Docking to Map Molecular Interactions of Steroid Analogs with Hepatic Organic Anion Transporting Polypeptides, J. Chem. Inf. Model. 61 (2021) 3109–3127. https://doi.org/10.1021/acs.jcim.1c00362.

[11] M.J. Abraham, T. Murtola, R. Schulz, S. Páll, J.C. Smith, B. Hess, E. Lindah, Gromacs: High performance molecular simulations through multi-level parallelism from laptops to supercomputers, SoftwareX. 1–2 (2015) 19–25.

[12] J. Huang, A.D. Mackerell, CHARMM36 all-atom additive protein force field: Validation based on comparison to NMR data, J. Comput. Chem. 34 (2013) 2135–2145. https://doi.org/10.1002/jcc.23354.

[13] W. Humphrey, A. Dalke, K. Schulten, VMD: Visual molecular dynamics, J. Mol. Graph. 14

(1996) 33–38.

[14] T. Kakiuchi, Y. Takasu, M. Senda, Voltage-Scan Fluorometry of Rose Bengal Ion at the 1, 2-Dichloroethane-Water Interface, Anal. Chem. 64 (1992) 3096–3100.

[15] N. Nishi, K. Izawa, M. Yamamoto, T. Kakiuchi, AC-modulated voltfluorometric study of the transient adsorption of rose bengal dianions in the transfer across the 1,2-dichloroethane|water interface, J. Phys. Chem. B. 105 (2001) 8162–8169.

[16] L. Poltorak, E.J.R. Sudhölter, L.C.P.M. de Smet, Effect of charge of quaternary ammonium cations on lipophilicity and electroanalytical parameters: Task for ion transfer voltammetry, J. Electroanal. Chem. 796 (2017) 66–74.

[17] G. Herzog, V. Kam, A. Berduque, D.W.M. Arrigan, Detection of food additives by voltammetry at the liquid-liquid interface, J. Agric. Food Chem. 56 (2008) 4304–4310.

[18] V.R. Batistela, D.S. Pellosi, F.D. De Souza, W.F. Da Costa, S.M. De Oliveira Santin, V.R. De Souza, W. Caetano, H.P.M. De Oliveira, I.S. Scarminio, N. Hioka, PKa determinations of xanthene derivates in aqueous solutions by multivariate analysis applied to UV-Vis spectrophotometric data, Spectrochim. Acta - Part A Mol. Biomol. Spectrosc. 79 (2011) 889–897.

[19] V. Gobry, S. Ulmeanu, F. Reymond, G. Bouchard, P.A. Carrupt, B. Testa, H.H. Girault, Generalization of ionic partition diagrams to lipophilic compounds and to biphasic systems with variable phase volume ratios, J. Am. Chem. Soc. 123 (2001) 10684–10690. https://doi.org/10.1021/ja015914f.

[20] F. Reymond, G. Steyaert, P.A. Carrupt, B. Testa, H. Girault, Ionic partition diagrams: A potential-pH representation, J. Am. Chem. Soc. 118 (1996) 11951–11957.

[21] F. Reymond, V. Chopineaux-Courtois, G. Steyaert, G. Bouchard, P.A. Carrupt, B. Testa, H.H. Girault, Ionic partition diagrams of ionisable drugs: pH-lipophilicity profiles, transfer mechanisms and charge effects on solvation, J. Electroanal. Chem. 462 (1999) 235–250.

[22] Z. Samec, Electrochemistry at the interface between two immiscible electrolyte solutions (IUPAC technical report), Pure Appl. Chem. 76 (2004) 2147–2180.

[23] D. Kuc-Ciepluch, M. Gorzkiewicz, E. Pędziwiatr-Werbicka, A. Barrios-Gumiel, M. Lasak, A. Mariak, K. Sztandera, R. Gomez, F.J. de la Mata, A. Lankoff, B. Klajnert-Maculewicz, M. Bryszewska, M. Arabski, K. Ciepluch, The effect of surface modification of dendronized gold nanoparticles on activation and release of pyroptosis-inducing pro-inflammatory cytokines in presence of bacterial lipopolysaccharide in monocytes, Colloids Surfaces B Biointerfaces. 217 (2022) 112652. https://doi.org/10.1016/j.colsurfb.2022.112652.

[24] A. Marczak, Fluorescence anisotropy of membrane fluidity probes in human erythrocytes incubated with anthracyclines and glutaraldehyde, Bioelectrochemistry. 74 (2009) 236–239.

[25] E.A. Zizzi, M. Cavaglià, J.A. Tuszynski, M.A. Deriu, Alteration of lipid bilayer mechanics by volatile anesthetics: Insights from μs-long molecular dynamics simulations, IScience. 25 (2022) 103946. https://doi.org/10.1016/j.isci.2022.103946.

[26] M. Klähn, M. Zacharias, Transformations in plasma membranes of cancerous cells and resulting consequences for cation insertion studied with molecular dynamics, Phys. Chem. Chem. Phys. 15 (2013) 14427–14441. https://doi.org/10.1039/c3cp52085d.

[27] G. Shahane, W. Ding, M. Palaiokostas, M. Orsi, Physical properties of model biological lipid bilayers: insights from all-atom molecular dynamics simulations, J. Mol. Model. 25 (2019) 1–13. https://doi.org/10.1007/s00894-019-3964-0.

[28] P.R. Maulik, G.G. Shipley, Interactions of N-stearoyl sphingomyelin with cholesterol and dipalmitoylphosphatidylcholine in bilayer membranes, Biophys. J. 70 (1996) 2256–2265. https://doi.org/10.1016/S0006-3495(96)79791-6.

[29] M. Saeedimasine, A. Montanino, S. Kleiven, A. Villa, Role of lipid composition on the structural and mechanical features of axonal membranes: a molecular simulation study, Sci. Rep. 9 (2019). https://doi.org/10.1038/s41598-019-44318-9.

[30] M.I. Yoguim, G.S. Grandini, L. de C. Bertozo, I. Caracelli, V.F. Ximenes, A.R. de Souza, Studies on the Interaction of Rose Bengal with the Human Serum Albumin Protein under Spectroscopic and Docking Simulations Aspects in the Characterization of Binding Sites, Chemosensors. 10 (2022) 440. https://doi.org/10.3390/chemosensors10110440.

[31] M. Niemi, Role of OATP transporters in the disposition of drugs, Pharmacogenomics. 8 (2007) 787–802.

[32] T. De Bruyn, S. Fattah, B. Stieger, P. Augustijns, P. Annaert, Sodium fluorescein is a probe substrate for hepatic drug transport mediated by OATP1B1 and OATP1B3, J. Pharm. Sci. 100 (2011) 5018–5030.

[33] M. Karlgren, A. Vildhede, U. Norinder, J.R. Wisniewski, E. Kimoto, Y. Lai, U. Haglund, P. Artursson, Classification of inhibitors of hepatic organic anion transporting polypeptides (OATPs): Influence of protein expression on drug-drug interactions, J. Med. Chem. 55 (2012) 4740–4763.

[34] D.G. Bailey, G.K. Dresser, B.F. Leake, R.B. Kim, Naringin is a major and selective clinical inhibitor of organic anion-transporting polypeptide 1A2 (OATP1A2) in grapefruit juice, Clin. Pharmacol. Ther. 81 (2007) 495–502.

[35] A. Kalliokoski, M. Niemi, Impact of OATP transporters on pharmacokinetics, Br. J. Pharmacol. 158 (2009) 693–705.

[36] O. Briz, M.R. Romero, P. Martinez-Becerra, R.I.R. Macias, M.J. Perez, F. Jimenez, F.G. San Martin, J.J.G. Marin, OATP8/1B3-mediated cotransport of bile acids and glutathione: An export pathway for organic anions from hepatocytes?, J. Biol. Chem. 281 (2006) 30326–30335.

[37] M. Schaefer, G. Morinaga, A. Matsui, G. Schänzle, D. Bischoff, R.D. Süssmuth, Quantitative expression of hepatobiliary transporters and functional uptake of substrates in hepatic two-dimensional sandwich cultures: A comparative evaluation of upcyte and primary human hepatocytes, Drug Metab. Dispos. 46 (2018) 166–177.

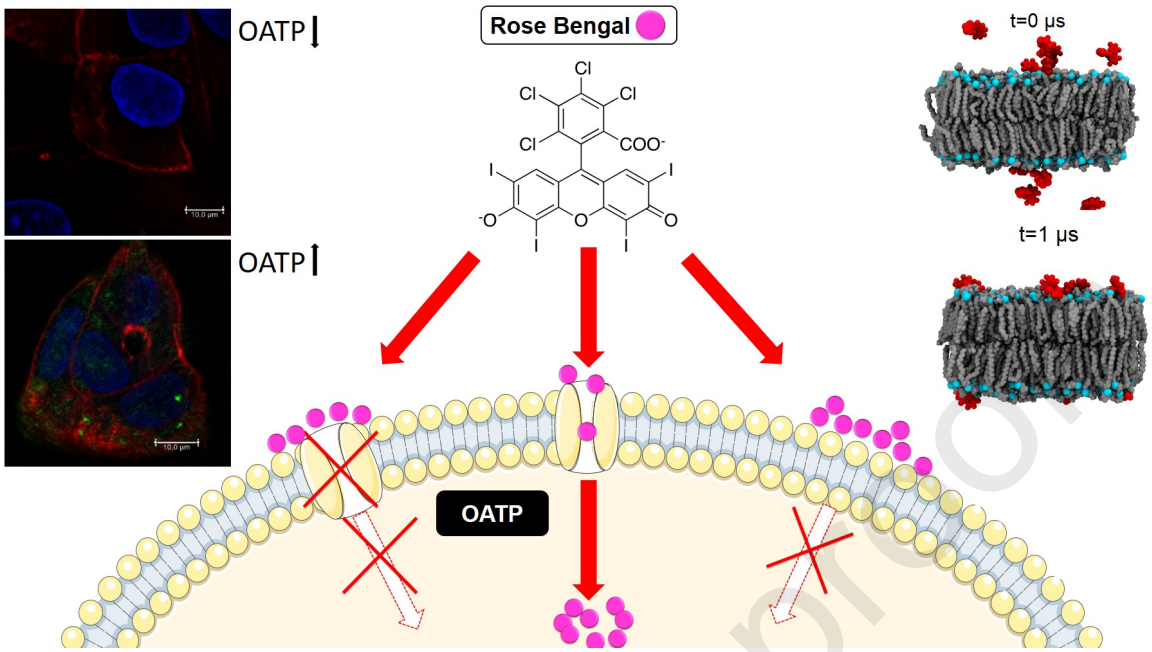

HIGHLIGHTS

- Rose bengal (RB) shows weak interactions with hydrophobic domains of lipid bilayer.
- RB interacts with the membrane surface, but cannot cross cellular membranes.
- Cellular uptake of RB requires activity of organic anion transporting polypeptides.

Declaration of interests

☒ The authors declare that they have no known competing financial interests or personal relationships that could have appeared to influence the work reported in this paper.

☐ The authors declare the following financial interests/personal relationships which may be considered as potential competing interests: